Check for updates

Thermally synthesized hematite (α-Fe₂O₃) nanoparticles as efficient photocatalyst for visible light dye degradation†

Sani Kundu,[a] Toton Sarkar,[a] Ahmad Aziz Al-Ahmadi,[b] Enas Ali[c] and Ashis Bhattacharjee ✶[a]

In recent years, water pollution has become a pressing global issue because of the continuous release of organic dyes from various industries. Therefore, finding an easy way to remove these harmful dyes from water has drawn the attention of researchers. This study investigates the removal of toxic Rose Bengal (RB) dye using hematite nanoparticles as a visible light photocatalyst without any additive. It is observed that by controlling particle size, quantity of the nanoparticles and reaction temperature, the dye degradation can be improved up to 95.33% with a half-life of 26 min. To understand photodegradation kinetic behavior, the Langmuir–Hinshelwood kinetic equation can be employed. The scavenger test indicated that the OH* radicals majorly led to the photodegradation process. The reaction rate values strongly depended on the size, quantity of the nanoparticles and reaction temperature. Controlling the optimizing condition, faster reaction rate ($k = 0.027$ min^{-1}) can be achieved as compared to earlier reports. It is also noted that the change in the degradation efficiency of the reused catalyst is negligible when compared to the fresh one. Here, the dye degradation mechanism is discussed. Overall, this study reveals that hematite nanoparticles can be used as efficient photocatalyst for dye degradation applications by optimizing the controlling factors. These observations provide novel perspectives on the development of effective and sustainable photocatalytic technologies for pollution control and water treatment applications.

1. Introduction

Hematite (α-Fe₂O₃) is a highly stable form of iron oxide. In its structure, Fe^{3+} ions occupy octahedral positions within a hexagonally close-packed lattice of oxygen atoms, forming a corundum crystal structure.[1] Being a transition metal oxide, hematite exhibits strong electron–electron correlation and electron–phonon coupling, which leads to complex electronic structures and appealing optical properties.[2] Below its Néel temperature of approximately 955 K, hematite exhibits canted ferromagnetic ordering. At around 263 K, it undergoes a Morin transition where the two magnetic sublattices align along the rhombohedral (111) axis and become exactly antiparallel. Hematite is classified as an n-type semiconductor (bandgap of 2.2 eV). In this material, the conduction band is characterized by empty Fe(III) d-orbitals, while the valence band is composed of occupied Fe(III) 3d crystal field orbitals partly mixed with O2p non-bonding orbitals.[3] When compared to their bulk counterparts, hematite nanoparticles exhibit unique properties that enhance their potential and indicate significant advancements in technological applications.[4] Due to its distinctive and significant properties, hematite at the nanoscale has received a lot of attention owing to its various applications, such as electronic, optical, and photonic devices.[5–7]

Water pollution is a pressing global issue primarily caused by the continuous release of synthetic dyes from various industries, with textile manufacturing being a significant contributor to dye pollution.[8–15] These colored dye substances are extensively used in industries, such as printing, dyeing, food, furniture, and paint. Shockingly, approximately 10–15% of these dyes are released into natural water sources without any treatment, posing a significant risk to ecosystems, human health, and aquatic life because of their extreme toxicity.[12,16–19] The non-biodegradable nature and complex aromatic structure of these hazardous organic dyes allow them to persist in the environment. Among the many dyes used in industry, Rose Bengal (RB) is particularly problematic to remove from wastewater. RB dye, a member of the xanthene group (Scheme 1), being carcinogenic is extremely hazardous. The aromatic
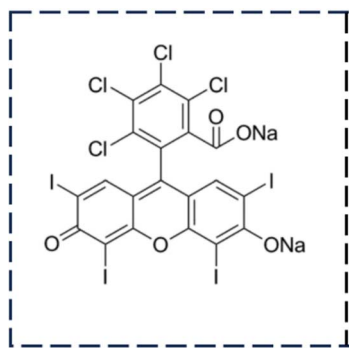
[a]Department of Physics, Visva-Bharati University, Santiniketan 731235, India. E-mail: ashis.bhattacharjee@visva-bharati.ac.in

[b]Department of Electrical Engineering, College of Engineering, Taif University, P. O. Box 11099, Taif 21944, Saudi Arabia

[c]Chitkara Centre for Research and Development, Chitkara University, Baddi, Himachal Pradesh, 174103, India

Scheme 1 Representation of the molecular structure of rose bengal.

groups combine the nucleus functions of xanthene, such as chromophore, which is used extensively throughout the world.[20] RB is an organic, water-soluble, anionic, photosensitive dye, unscented and dark pink powder widely used in textiles, antimicrobial therapy, plastic, food, pharmaceutics, cosmetics, and printing.[21,22] Exposure to this dye can lead to adverse health effects such as irritation, reddening, blistering of the skin, and severe corneal epithelium damage.[22–25] Sako and co-workers[26,27] studied the toxic effect of RB. Although considerable advances have already been made in the degradation of dyes, the degradation of RB has been less explored. Moreover, previous reports involved longer times for the degradation of RB. Bhar et al.[28] studied the degradation of RB using nanocrystalline FeS_2 thin films and observed 84% degradation of dye solution in 300 min. The degradation of RB has been studied by Farbod and Khademalrasool[29] using TiO_2 nanoparticles. Complete degradation of the dye was observed at 210 min. Similarly, Vignesh et al.[30] observed 85% degradation of RB in 150 min with Ag-doped SnO_2 nanoparticles modified with curcumin. Therefore, the urgent need to eliminate this toxic RB dye from water resources has driven the scientific community to explore various removal methods.

Traditional approaches, such as adsorption, coagulation, membrane separation, and ion exchange processes, have limitations such as high costs, slow operation, and generation of toxic byproducts.[31] In this context, utilizing metal oxide semiconductors for photocatalytic degradation has emerged as a promising method due to their surface area to volume ratio, chemical stability, and high photocatalytic activity of these materials.[32–38] Photocatalytic reactions involve three main processes: (i) the creation of electron–hole pairs through photoexcitation, (ii) the transport of carriers to the catalytic surface, and (iii) the occurrence of chemical reactions on the surface.[38] Establishing the photocatalyst's stability and activity is essential for any photocatalytic system. In addition to the catalyst's activity, various factors, such as pH, temperature, size, amount of catalyst, and charge of the pollutant, have also been found to influence degradation efficiency.[39] Thus, the optimization of these factors can be considered an effective way to achieve maximum efficiency while developing and producing multifunctional semiconductor photocatalysts for the photocatalytic treatment of organic contaminants. Among the

different metal oxides, hematite can serve as an effective photocatalyst for the photocatalytic degradation of several toxic dyes,[40] such as malachite green,[41] salicylic acid,[42] methylene blue,[43–51] methyl orange,[49,52–54] atrazine,[55] rhodamine B,[55–58] Congo red,[52,59,60] and rose bengal.[60–66] The photodegradation efficiency and rate constant of the hematite nanoparticles for different dyes reported in the literature are presented in Table 1.

Recently, we reported the synthesis of hematite nanoparticles of 25 and 55 nm sizes using malonic acid ($C_3H_4O_4$) and glucose ($C_6H_{12}O_6$), respectively, as co-precursors in various weight ratios on the thermal decomposition of iron(III)citrate at a comparatively lower temperature in an ambient atmosphere.[69] Additionally, Mössbauer, magnetization and Raman studies were performed to identify the purity of these hematite nanoparticles. Different electronic transitions existing in the hematite materials were identified by UV-Vis-NIR absorption study, and the direct (1.95–1.99 eV) and indirect (1.4–1.5 eV) energy band gaps were determined. Several defect levels were found inside the energy band gap (1.39, 1.40, 1.63, and 1.67 eV) in the photoluminescence study. These hematite nanomaterials exhibit large dielectric constant values with low dielectric loss values depending on the particle size.[70]

In the present study, we investigate the photocatalytic degradation of RB dye using these well-characterized thermally synthesized hematite nanoparticles. The aim is to understand the effect of particle size, quantity of catalyst and reaction temperature on the RB dye degradation efficiency. The associated reaction kinetics and the mechanism of the dye degradation have been discussed. By studying the interaction between dyes and hematite nanoparticles, we aim to contribute valuable insights to the field of nanomaterial-based environmental technology and additive-free water treatment applications.

2. Materials and methods

For photocatalytic degradation studies, we used thermally synthesized 25 nm and 55 nm hematite samples, which are named H25 and H55 hereinafter. The synthesis and characterization of these materials have been reported in previous studies.[69] The rose bengal (≥80%) dye was purchased from Sigma-Aldrich (Japan). In the photocatalytic experiment, a 250 W Hg(Xe) light source from Newport Corporation, USA, was utilized. Hematite nanoparticles were added in varying amounts (30 mg, 60 mg, and 90 mg) to 100 mL of aqueous solutions containing 10 ppm of RB dye. The solutions were stirred in the dark for 1 h to facilitate dye adsorption onto the α-Fe_2O_3 nanoparticles (H25 and H55). Subsequently, the solutions were exposed to the light source at room temperature by placing them 25 cm away from the light source. The degradation of the dye aqueous solution was recorded using a Beckman DU® 720 UV/Vis spectrophotometer by collecting samples at regular intervals after centrifuging for 15 min. To test the photocatalytic performance of the present samples, RB dye is degraded over time under the irradiation of Hg(Xe) light. The dye degradation percentage is estimated as follows:

$$\% \text{ Degradation} = (C_0 - C)/C_0;$$

Table 1 Photocatalytic activity of some hematite nanostructures[a]

Morphology of the catalyst	Synthetic method	Size (nm)	Dye	Dye weight/ catalyst weight	Maximum degradation (%)	Pseudo-first-order rate constant (k) (min^{-1})	References
Nanoparticles	Combustion	48	Malachite green	1×10^{-2}	46.29	3.3×10^{-3}	41
Hollow sphere	Hydrothermal	50–60	Salicylic acid	2.5×10^{-1}	70		42
Silkworm cocoon-like	Hydrothermal	20	MO	3×10^{-3}	83.9		52
Nanoparticles	Thermal decomposition	34.5	MO	7.5×10^{-2}	91	2.7×10^{-2}	49
Nanoparticles	Co-precipitation	44	MO	1×10^{-3}	67.8		54
Nanoparticles	Green synthesis	34	MO	1.4×10^{-2}	15		51
Nanoparticles	Combustion	27.2	MO	2×10^{-2}	28	2.2×10^{-3}	53
Nanoparticles	Polymeric precursor	20–32	Atrazine	1×10^{-2}	59		55
Porous nanorods	Chemical	120	RhB	3.3×10^{-2}	97		56
Nanostructures	Solvothermal	30–100	RhB		80–90		57
Nanoparticles	Polymeric precursor	20–32	RhB	1×10^{-2}	40		55
Nanoparticles	Combustion	63–71	RhB	1×10^{-2}	48–57	4.8×10^{-3}	58
Nanobraids and nanoporous	Electrospinning	20–40	CR	8×10^{-2}	91.2		59
Nanoparticles	Chemical	12–26	CR	4×10^{-2}	16.92	0.564×10^{-2}	60
Nanoparticles	Chemical	12–26	CR	4×10^{-2}	99.3	4.22×10^{-2}	60
Silkworm cocoon-like	Hydrothermal	20	CR	2×10^{-3}	99.2		52
Nanoparticles	Thermal decomposition	34.5	MB	7.5×10^{-2}	97	4×10^{-2}	49
Nanoparticles	Sol–gel auto-combustion	50	MB	5×10^{-2}	73	7.9×10^{-3}	43
Nanoparticles	Green synthesis	16–35	MB	1×10^{-1}	78.68	1.08×10^{-2}	44
Nanoparticles	Green synthesis	33	MB	3.2×10^{-3}	76		50
Nanoparticles	Green synthesis	34	MB	1.4×10^{-2}	50	3.84×10^{-3}	51
Nanoparticles	Co-precipitation	42	MB	5×10^{-3}	92		67
Porous nanorods	Hydrothermal	2–4	MB	1.5×10^{-2}	90	1.04×10^{-2}	68
Nanoparticles	Hydrothermal	26.2	MB	1.5×10^{-2}	33	0.33×10^{-2}	45
Nanoparticles	Chemical	21.1	MB		92.3		46
Nanoparticles	Sol–gel	13.4	RB	1×10^{-2}	58		61
Nanoparticles	Thermal decomposition	19–27	RB	9.3×10^{-2}	98	2.65×10^{-2} 1.57×10^{-2}	62
Nanoparticles	Sol–gel	15	RB	5×10^{-3}	63	1.087×10^{-2}	63
Nanoparticles	Sol–gel	33.7	RB	1×10^{-1}	7.3	0.14×10^{-2}	64
Nanoparticles	Hydrothermal	12.6	RB	5×10^{-3}	75	1.907×10^{-2}	12
Nanoparticles	Green synthesis	25.65	RB	2.4×10^{-2}	90.99		65
Nanoparticles	Chemical	12	RB	4×10^{-2}	98.7	3.14×10^{-2}	60
Nanoparticles	Chemical	26	RB	4×10^{-2}	62.5	0.46×10^{-2}	60
Nanoparticles	Chemical	25.10	RB	4×10^{-2}	62.9	1.58×10^{-2}	66

[a] MO-methyl orange, RB-rose bengal, MB-methylene blue, RhB-rhodamine B, CR-Congo red.

where C = the dye concentration at a given reaction time t and C_0 = the initial concentration of aqueous dye. These experiments were repeated at different steady temperatures.

Photocatalytic experiments with scavengers were performed with 30 mg of H25 photocatalyst of 100 mL 10 ppm RB solution. Isopropyl alcohol ($\geq$99%), potassium dichromate ($K_2Cr_2O_7$) ($\geq$99%) and ethylene diamine tetra-acetic acid disodium (EDTA-2Na) ($\geq$99%) were used as effective scavengers for the OH*, O_2^{*-}, and h^+ radicals, respectively. Initially, 1 mM per L aq. solutions of $K_2Cr_2O_7$ and EDTA-2Na were prepared individually. Different amounts of scavenger solutions (2 and 5 mL) were added to the dye solution containing the photocatalyst and RB. Before illumination, the solutions were stirred in the dark for 1 h.

3. Results and discussion

The surface area, atomic structure, and electronic structure of nanoparticles have a significant impact on their photocatalytic activity. The synthesized hematite nanomaterials (H25 and
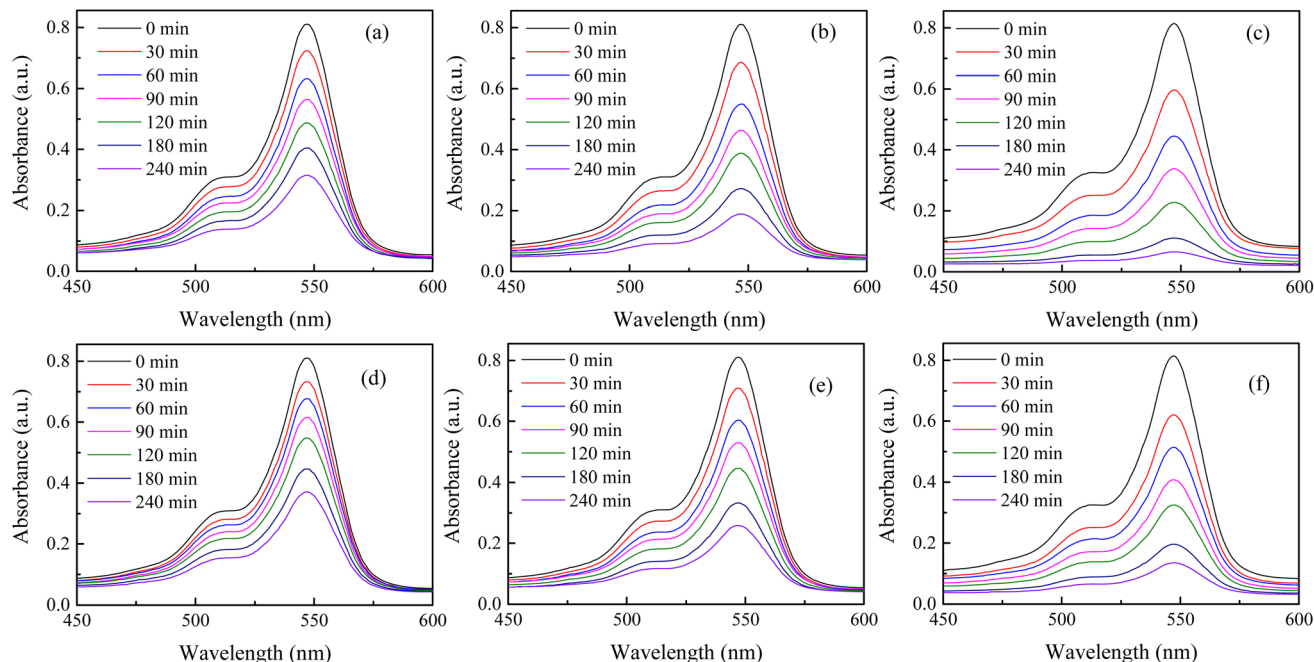
Fig. 1 Room temperature time-dependent spectral change in RB solution with (a) 30 mg, (b) 60 mg, and (c) 90 mg of H25 as the catalyst and (d) 30 mg, (e) 60 mg, and (f) 90 mg of H55 as the catalyst.

H55) have a band gap energy (1.60–2.03 eV)[69] that falls in the visible region of the electromagnetic spectrum, indicating that the photocatalytic degradation process should occur under visible light. The room temperature time-dependent absorption spectra of the RB solution catalyzed by various amounts of H25 and H55 nanoparticles are displayed in Fig. 1. From these figures, it can be observed that the intensity of the characteristic peak for RB at 547 nm decreases with time in all cases. The degradation percentages of RB solution are noted as 61.16%, 76.7%, and 92.27% with 30, 60 and 90 mg of H25 as the catalyst, whereas 54.26%, 68.19%, and 83.44% with 30, 60 and 90 mg of H55 as the catalyst, respectively. Thus, photodegradation increases with a smaller size and with an increasing amount of hematite catalyst. Fig. 2 depicts the time-dependent degradation of RB solution catalyzed by 90 mg of H25 obtained at room temperature through color change. It is evident from this figure that the vibrant pink color of RB gradually fades into a colorless

state as a result of exposure to light. This observation highlights the impact of H25 as a catalyst on the degradation of RB dye under light-induced conditions, leading to the loss of its characteristic color. Furthermore, from the absorption studies that maintain the RB dye solution in the dark at different temperatures (ESI†), it is found that the intensity of the RB dye solution in the presence of a catalyst remains unaffected by temperature. This observation indicates that no thermal reaction occurred to initiate any degradation.

A comparison of catalytic performance at room temperature between H25 and H55 in Fig. 3(a) illustrates that for any fixed amount of photocatalyst, H25 shows higher catalytic activity than H55. This finding indicates the significant impact of particle size on the efficiency of dye degradation. Therefore, for the present study, it is noteworthy that smaller catalysts show enhanced responses, which is in agreement with previous studies on various types of catalysts. For instance, Lin et al.[71] demonstrated a dependency of particle size on the electro-optical properties of catalysts, showing that as the catalyst size increases, the photocatalytic rate constant exponentially decreases. Similarly, Cheng et al.[72] described that the photocatalytic activity of AgI/BiOI photocatalysts is size dependent, with enhanced activity observed for smaller AgI nanoparticles. This phenomenon is attributed to the existence of a greater number of surface-active sites and faster spatial charge transfer in smaller particles. In the case of H25, the smaller particle size results in a larger surface area to volume ratio available for catalytic reactions to occur. This number of active sites increases the interactions between dye molecules and the catalyst, leading to a higher rate of dye degradation.[73] Furthermore, the smaller particle size of H25 facilitates the quicker transfer of photogenerated carriers to the sample surface
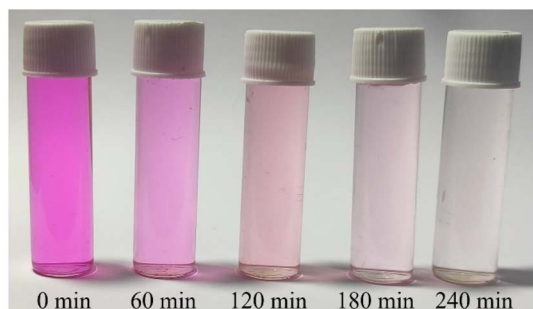

Fig. 2 Room temperature time-dependent degradation of RB solution catalyzed by 90 mg of H25.
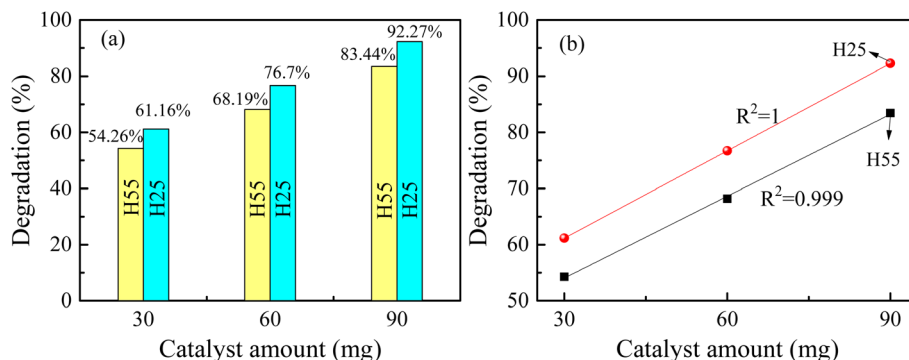
Fig. 3 (a) Variation in degradation efficiency with catalyst size and amount at room temperature. (b) Nature of variation in degradation of RB solution for H25 and H55 with catalyst amount at room temperature.

without recombination.[74] This efficient charge transfer process contributes to the enhanced catalytic performance of H25 compared to H55. Overall, these findings highlight the importance of particle size in influencing the catalytic activity of photocatalysts and emphasize the impact of surface area and charge transfer dynamics in driving efficient dye degradation processes.

From Fig. 3(b), it is evident that the photocatalyst amount influences the dye degradation process. It is noted that as the amount of catalyst increases, the degradation percentage also increases linearly (see Fig. 3(b)). Similar results have been observed in previous studies.[75–78] Presently, the linear increase in degradation with increasing catalyst amount indicates a direct correlation between catalyst quantity and dye degradation. Fitting the experimentally obtained data linearly, the degradation percentages can be mathematically expressed as follows:

$$\text{Degradation (\%)} = 45.6 + (0.5185 \times \text{catalyst amount}) \text{ for H25,} \quad \text{(i)}$$

$$\text{Degradation (\%)} = 39.45 + (0.48633 \times \text{catalyst amount}) \text{ for H55.} \quad \text{(ii)}$$

The increase in the total available surface area associated with the catalyst as a result of higher quantity promotes greater adsorption of dye molecules. This improved adsorption capacity facilitates a more efficient interaction between the dye molecules and the catalyst, leading to enhanced degradation of the dye molecules in the RB solution. As the amount of photocatalyst increases, the active sites available on the catalyst surface for catalytic reactions to occur also increase.[79] This greater number of active sites promotes the creation of additional photogenerated electron–hole pairs, which are vital to producing hydroxyl radicals responsible for dye degradation.[79] Therefore, increasing the number of photocatalysts results in a larger surface area, improved adsorption capacity, and a higher number of active sites, all of which contribute to the enhanced degradation efficiency of dye molecules in the RB solution. It is observed that 90 mg of H25 hematite nanoparticles shows better photodegradation of RB dye solution. Therefore, this is chosen for further research.

Time-dependent spectral changes in 10 ppm 100 mL RB solution catalyzed by 90 mg of H25 hematite nanoparticles at 50 °C and 70 °C are displayed in Fig. 4(a) and (b), respectively. After 240 min of light irradiation, the degradation efficiencies
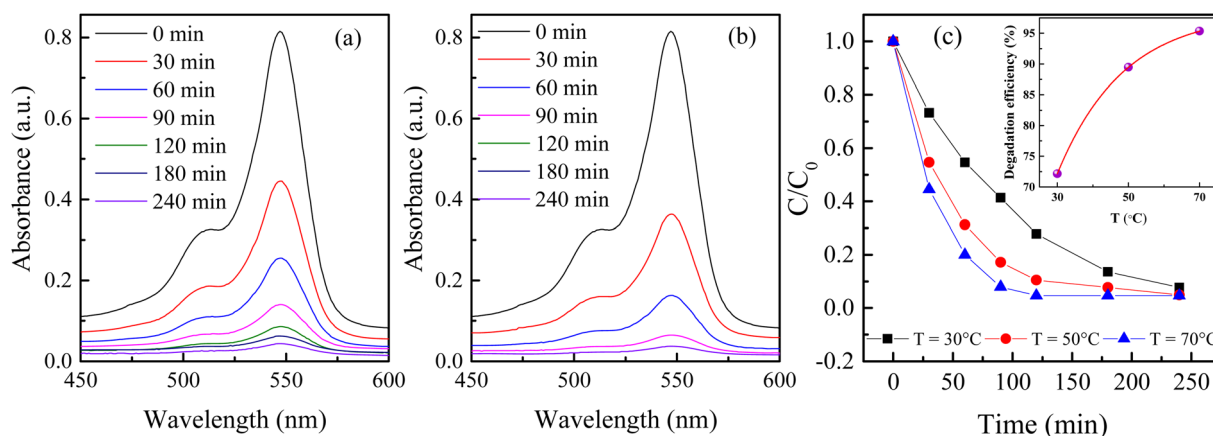

Fig. 4 Time-dependent spectral change in RB solutions catalyzed by 90 mg of H25 hematite nanoparticles at (a) 50 °C and (b) 70 °C; (c) variation in degradation with time at different steady temperatures; inset shows the variation in degradation efficiency with temperature 120 min after the irradiation of light.

are noted as 95.09% and 95.33% at 50 °C and 70 °C, respectively. Under the same conditions at room temperature, the degradation efficiency was 92.27%. Fig. 4(c) shows the variation in degradation of RB solution catalyzed by 90 mg of H25 with time at different steady temperatures, and the figure inset shows the variation in degradation efficiency with temperature after 120 min of light irradiation. From this figure, the impact of temperature on the degradation of RB solution can be better understood. It is evident that the change in efficiency after 240 min is very small, but with an increase in temperature, the degradation becomes much faster. For instance, the degradation percentage after 120 min of light irradiation is 72.15% at room temperature, which becomes 89.45% at 50 °C and 95.33% at 70 °C. The inset in Fig. 4(c) indicates that the degradation efficiency exponentially increases with increasing temperature after 120 min of irradiation of light. Therefore, it is noted that the degradation efficiency increases significantly as the reaction temperature increases. There are no reports on the temperature dependency of RB solution in the presence of a hematite catalyst found in the literature. The effect of water temperature on titanium dioxide's photocatalytic activity was investigated by Janus et al.[80] It was demonstrated that one explanation for the temperature-dependent increase in photocatalytic activity might be that as the water temperature increases, the concentration of hydroxyl radicals in the water increases because of the increase in the ionic product of water. It has been described that an increase in efficiency is linked to an increase in the water's ionic product, which increases with temperature and increases the hydroxyl ion concentration. According to Meng et al.,[81] a higher reaction temperature substantially encourages dye molecule mobility, making it easier for the molecules to pass through the material's micropores.

Kinetic study

The kinetic study is crucial for the removal process of pollutant dye molecules from waste water to be used on a larger scale.[82] To understand the photodegradation kinetic behavior, the Langmuir–Hinshelwood kinetic equation can be employed.[83,84] According to the Langmuir–Hinshelwood kinetic equation,[85] first order (eqn (1)) and second order (eqn (2)) kinetic equations can respectively be represented as follows:

$$-\ln\left(\frac{C}{C_0}\right) = kt + \text{constant} \quad (1)$$

and

$$\frac{1}{C} = k't + \text{constant}, \quad (2)$$

where C_0 denotes the initial concentration and C denotes the concentration at t time. The first order rate constant (k, min^{-1}) and the second order rate constant (k', min^{-1}) can be determined from the slope of the plot $-\ln\left(\frac{C}{C_0}\right)$ vs. t and $1/C$ vs. t, respectively. Moreover, the half-life ($t_{1/2}$), which indicates the time taken for the initial dye concentration to reduce by half of the reactions, can be calculated using eqn (3) as follows:

$$t_{1/2} = \frac{\ln(2)}{k} = \frac{0.693}{k}. \quad (3)$$

The degradation plots following eqn (1) and (2) for different amounts of H25 and H55 at room temperature are shown in Fig. 5 and 6, respectively. Estimated first-order and second-order reaction rate constants for varying catalyst size, amount and solution temperature following eqn (1) and (2) are presented in Table 2. From this table, it is evident that first-order kinetic linear regression (R^2) coefficient values are closer to unity than those for second-order kinetic for all cases, which elucidates that the degradation processes may be described better by the first-order kinetic i.e., eqn (1). Table 2 also displays the half-life values that were determined using first-order kinetics.

Fig. 7(a) shows the variation in the reaction rate constant with size at room temperature. From this figure, nanoparticles with smaller sizes for any fixed catalyst amount exhibit a higher reaction rate for the photo degradation of RB. This can be described by the fact that a smaller-sized catalyst has a larger surface to volume ratio compared to a bigger-sized catalyst, resulting in a greater number of active sites. Therefore, a greater number of dye molecules can interact with the catalyst simultaneously, leading to a faster rate of degradation. Furthermore, the decreased size of the photocatalyst may have an impact on the number of catalysts for any fixed amount of mass. For
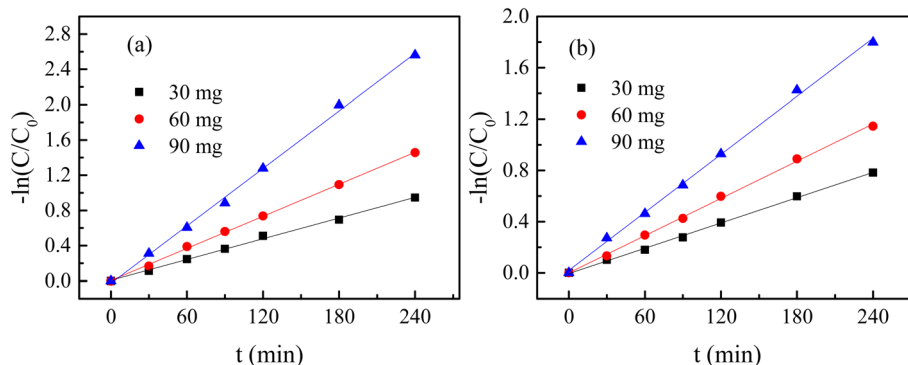

Fig. 5 $-\ln\left(\frac{C}{C_0}\right)$ vs. t plots for different amounts of catalyst at room temperature: (a) H25 and (b) H55.
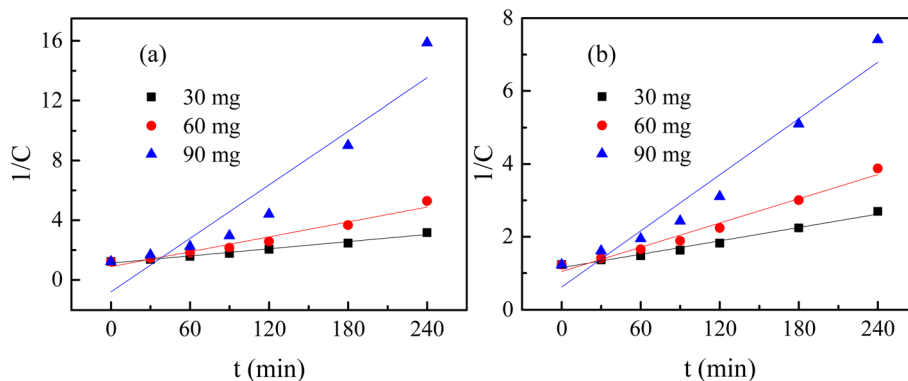
Fig. 6 $\frac{1}{c}$ vs. t plots for different amounts of catalyst at room temperature: (a) H25 and (b) H55.

smaller particles, more nanoparticles are present in the solution to drive the degradation process, enhancing the reaction rate. Additionally, a higher surface area is useful for adsorbing radiation, which produces more holes and electrons.[86,87] Consequently, the number of carriers increases, leading to an increase in the reaction rate. Thus, enhanced absorption capacity leads to improved photocatalytic activity.

Fig. 7(b) shows the variation in the reaction rate constant with the catalyst amount at room temperature. It is noted that for any particular material increasing the catalyst amount leads

to an increase in reaction rate linearly. A higher concentration of catalysts provides a greater number of active sites with which the dye molecules can react. Consequently, more dye molecules can be degraded simultaneously, leading to a faster reaction rate. Furthermore, a higher concentration of the photocatalyst in the solution can enhance the probability of collisions among the dye molecules and the catalyst, which can further contribute to the faster reaction rate.

The degradation plots following eqn (1) and (2) for 90 mg of H25 under different temperatures are presented in Fig. 8(a) and

Table 2 Reaction rate values for different sizes and amounts of catalyst and reaction temperature

Sample	Size (nm)	Temperature (°C)	Amount (mg)	First order, eqn (1)			Second order, eqn (2)	
				Reaction rate, k ($\times 10^{-2}$)	R^{2a}	$t_{1/2}$ (min)	Reaction rate, k' ($\times 10^{-2}$)	R^{2a}
H25	55	30	30	0.324	0.998	214	0.614	0.980
		30	60	0.485	0.999	143	1.111	0.975
		30	90	0.778	0.997	89	2.572	0.940
H55	25	30	30	0.4	0.997	173	0.799	0.980
		30	60	0.614	0.999	113	1.664	0.960
		30	90	1.036	0.998	67	5.972	0.896
		50	90	1.955	0.999	35	8.566	0.927
		70	90	2.7	0.999	26	20.936	0.897

[a] R^2 provides the quality of fit of plots in Fig. 5, 6 and 8.
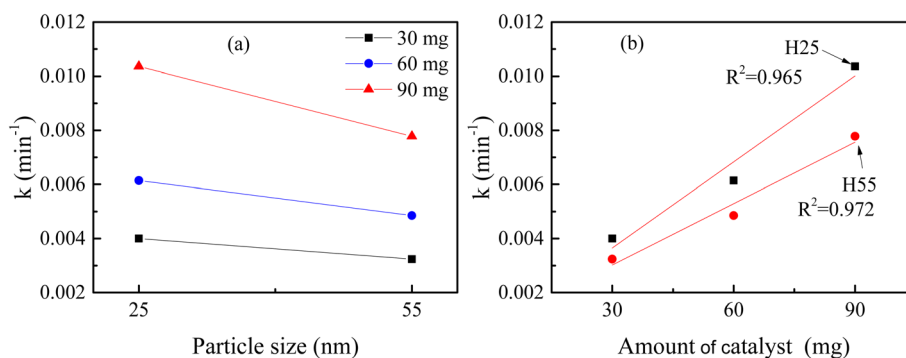

Fig. 7 Variation in reaction rate constant at room temperature with (a) particle size and (b) amount of catalyst.
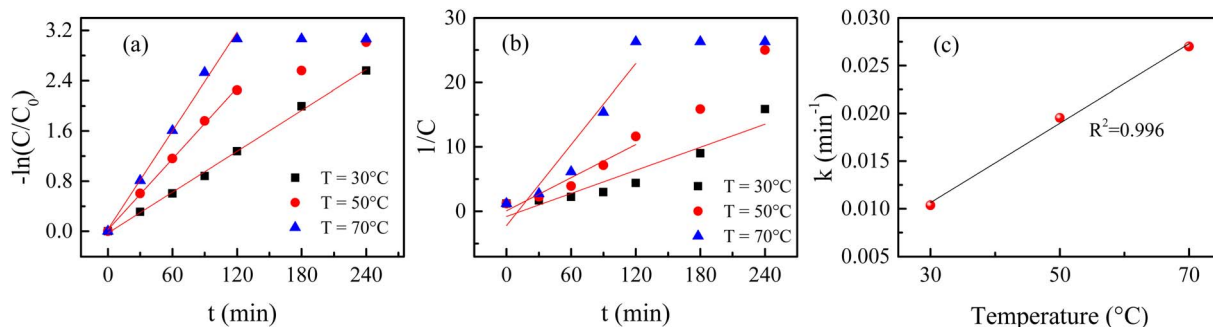

Fig. 8 (a) $-\ln\left(\frac{C}{C_0}\right)$ vs. t plots, (b) $1/C$ vs. t plots and (c) variation in the reaction rate constant for 90 mg of H25 under different temperatures.
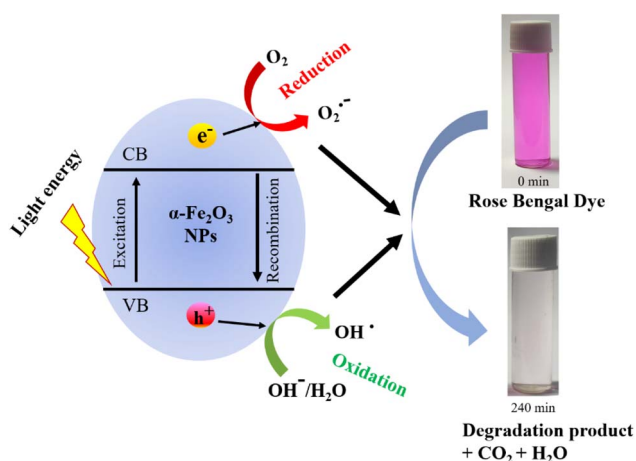
(b), respectively. From Table 2, it is evident that the degradation processes can be described more accurately by the first-order kinetic equation, *i.e.*, eqn (1), at elevated temperatures too. Fig. 8(c) depicts the variation in the reaction rate constant with temperature. It is noted that with an increase in solution temperature, the reaction rate also increases linearly. This can be understood by the fact that higher temperatures provide more energy for the reactant molecules, which increases their kinetic energy. Consequently, the number of collisions between the catalyst and dye molecules increases, leading to an increased reaction rate.

Thus, it is observed that catalyst particle size, catalyst quantity, and solution temperature have a significant impact on determining the reaction rate of the photodegradation process of RB dye molecules in aq. solution using hematite nanoparticles as catalysts. Optimizing these factors can lead to enhanced efficiency in the degradation of the rose bengal dye using hematite nanoparticles.
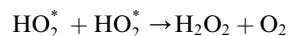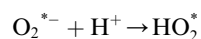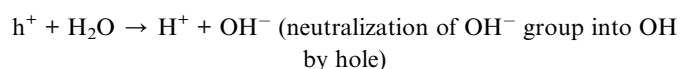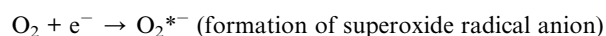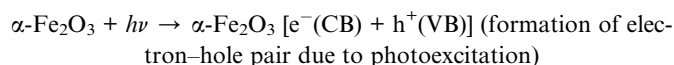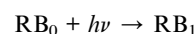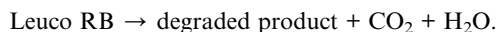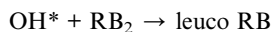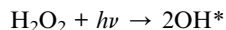
Mechanism of dye degradation

The mechanism of RB dye degradation using hematite nanoparticles as photocatalysts is presented in Scheme 2. The mechanism of light-induced degradation of RB using a hematite (α-Fe_2O_3) catalyst involves an advanced oxidation process.[88] When photons are absorbed by the photosensitive RB dye, they transition to an excited singlet state (RB_1), followed by conversion to an excited triplet state (RB_2) through intersystem crossing (ISC).[88] Upon irradiation, α-Fe_2O_3 excites electrons from the valence band to the conduction band, creating electron (e^-)/hole (h^+) pairs. The generated electrons interact with adsorbed O_2 molecules to form superoxide anion O_2^{*-} radicals, leading to the production of HO_2^* in the presence of water. Moreover, the holes generate OH^- radicals when they interact with surface OH^- groups.[89-91] O_2^- can act as an oxidizing agent and provide an additional source of OH radicals. H_2O_2 is produced as an intermediate product during the reaction, absorbing electrons to produce (OH*). A Fenton-like process may occur, where Fe^{2+} ions react with H_2O_2 to produce (OH*) radicals.[89] These (OH*) and (O_2^{*-}) radicals have a significant impact on degrading the dye molecules by oxidizing them to their colorless leuco form and eventually to harmless compounds.[88] Consequently, the RB dye can be effectively broken down into non-toxic organic compounds, such as CO_2 and H_2O, by these hydroxyl radicals. Furthermore, organic pollutants adsorbed on the photocatalyst's surface can be directly oxidized.[92] In conclusion, the oxidative (using holes) and reductive (using electrons) pathways of the photocatalytic degradation reaction employing hematite can be summarized as follows:[88,93,94]

$$RB_0 + h\nu \rightarrow RB_1$$

$$RB_1 \rightarrow RB_2; \text{ (inter system crossing)}$$

$$\alpha\text{-}Fe_2O_3 + h\nu \rightarrow \alpha\text{-}Fe_2O_3 \; [e^-(CB) + h^+(VB)] \text{ (formation of electron–hole pair due to photoexcitation)}$$

$$O_2 + e^- \rightarrow O_2^{*-} \text{ (formation of superoxide radical anion)}$$

$$h^+ + H_2O \rightarrow H^+ + OH^- \text{ (neutralization of } OH^- \text{ group into OH by hole)}$$

$$O_2^{*-} + H^+ \rightarrow HO_2^*$$

$$HO_2^* + HO_2^* \rightarrow H_2O_2 + O_2$$

Scheme 2 Mechanism of rose bengal dye degradation.

$$H_2O_2 + h\nu \rightarrow 2OH^*$$

$$OH^* + RB_2 \rightarrow \text{leuco RB}$$

$$\text{Leuco RB} \rightarrow \text{degraded product} + CO_2 + H_2O.$$

Scavenger activity

The involvement of several active species in the photodegradation of RB dye is examined using radical trapping or scavenger activity study (see ESI† for observed absorption spectra in the presence of different scavengers). To determine reactive species present during the photodegradation of RB dye, different scavengers were used. Fig. 9 illustrates the scavenger activity in the RB dye solution in the presence of H25 nanoparticles. The scavengers trap the reactive species and decrease their production. Here, isopropyl alcohol (IPA), potassium dichromate ($K_2Cr_2O_7$) and ethylene diamine tetra acetic acid disodium (EDTA-2Na) are used as effective scavengers for the OH^*, O_2^{*-}, and h^+ radicals, respectively. Initially, without any scavenger, a degradation of 61.16% was observed with 30 mg of H25 catalyst at room temperature. However, when 2 mL of

Fig. 9 Scavenger activity observed for photodegradation of RB with 30 mg of H25 catalyst at room temperature.

scavenger was introduced, the degradation decreased to 34.73% for IPA, 40.87% for $K_2Cr_2O_7$, and 47.34% for EDTA-2Na. This reduction suggests that these scavengers inhibit the degradation process by quenching the reactive species responsible for dye degradation. The effect becomes more pronounced when the scavenger volume was increased to 5 mL, resulting in a further decrease in the degradation rate to 7.75%, 17.24%, and 21.26% for IPA, $K_2Cr_2O_7$, and EDTA-2Na, respectively. This reveals that without scavengers, photodegradation of RB dye shows the highest percentage of degradation. There is a significant reduction in the photodegradation efficiency of RB dye observed in the presence of these scavengers, among which IPA exhibited the strongest effect. This result indicates that although all three radicals OH^*, O_2^{*-}, and h^+ play a role in the photodegradation of RB, the OH^* radicals are majorly responsible for the photodegradation process.

Reusability of the catalyst

To check the reusability of the photocatalyst sample, after the use of 90 mg H25 in 100 mL of aqueous solutions containing 10 ppm of rose bengal, the used sample was filtered and collected after drying. 64 mg sample was recovered, out of which a 60 mg sample was used again for the same experiment (say, recycle-1). Similarly, after recycle-1, the used sample was filtered and collected after drying. 35 mg of sample was recovered, out of which 30 mg sample was used again for the same experiment (say, recycle-2). Fig. 10(a) and (b) depict the time-dependent spectral change in RB solution for recycle-1 and recylce-2 with H25 at room temperature, respectively. Fig. 10(c) illustrates a comparison of the degradation percentages for the fresh sample with the recycled sample. It is observed that with 60 mg of H25, the degradation percentage is 76.7% for the fresh sample and 75.84% for recycle-1. Moreover, the degradation percentage with the 30 mg fresh sample is 61.16%, while that for recycle-2 is 60.5%. Therefore, it is very clear that in comparison to the fresh sample, the change in the photocatalytic performance of the recycled nanoparticles was negligible. Thus, it is observed that after multiple reuses, the dye degradation performance of the recycled nanoparticles remained nearly unchanged. To verify any change in the structure of the catalyst, powder XRD patterns of H25 before and after photocatalysis were obtained and analyzed (see ESI†).
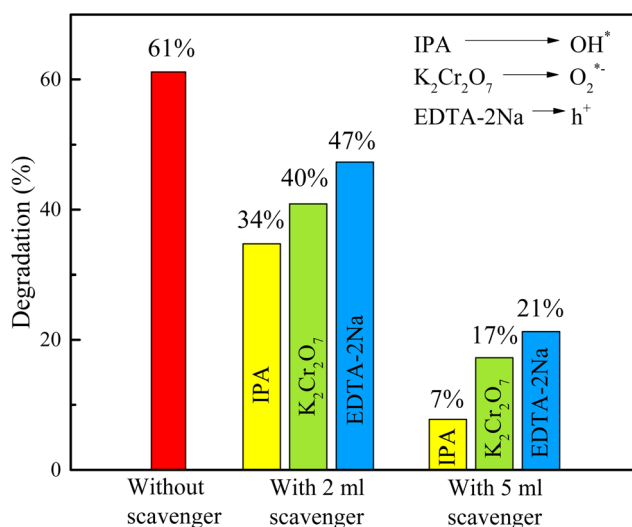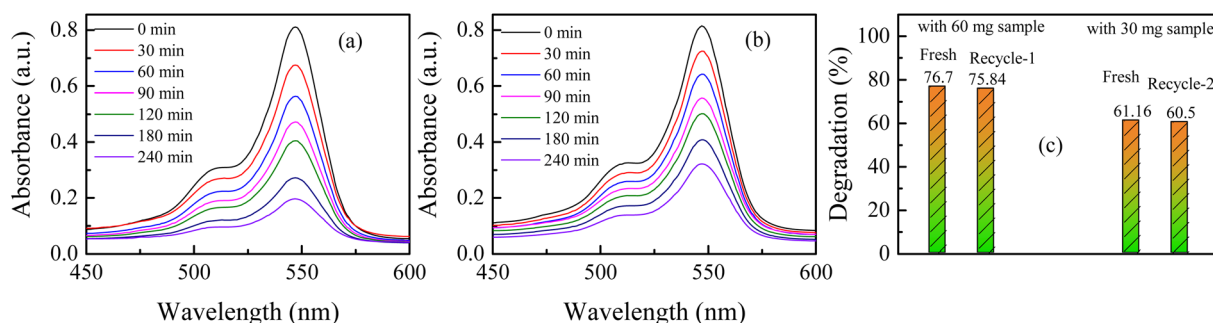

Fig. 10 Time-dependent spectral change in RB solution with H25 at room temperature: (a) recycle-1, (b) recylce-2; (c) comparison of degradation efficiency for recycle-1 and recycle-2 with fresh catalyst.

The similarity between the two XRD patterns and the values of the estimated parameters for both samples confirmed that the hematite nanoparticles used as photocatalysts for dye degradation did not suffer any structural change even after their repeated use in photocatalysis.

4. Conclusions

In the present study, the role of thermally synthesized hematite nanoparticles in the photocatalytic activity of rose bengal dye is investigated. The study demonstrated that smaller hematite nanoparticles exhibit superior photocatalytic activity because their higher surface area-to-volume ratio supplies a greater number of active sites for dye degradation. Furthermore, increasing the catalyst amount led to an improvement in the degradation percentage due to an increase in the available active sites. It is also observed that an increase in reaction temperature increases the degradation efficiency. Under optimized conditions, a 95.33% degradation efficiency can be achieved with a half-life of 26 min using thermally synthesized hematite nanoparticles. The nature of the dye degradation is understood following Langmuir–Hinshelwood first-order and second order equations, where the first order equation is found to be more suitable for describing the dye degradation processes. The scavenger test shows that although all three radicals, OH^*, O_2^{*-}, and h^+, play a role in the photodegradation of RB, the OH^* radicals are the majorly responsible ones. The estimated reaction rate constant values depend on various factors such as size, quantity of the photocatalyst and reaction temperature. Under optimized conditions, a faster reaction rate ($k = 0.027$ min^{-1}) can be achieved compared to earlier reports. The reusability of the photocatalyst has been explored and it is observed that the change in degradation efficiency for the reused sample is negligible compared to the fresh one; moreover, the degradation mechanism has been explored. The findings reveal that the thermally synthesized hematite nanoparticles are promising candidates as photocatalysts in the water treatment process and environmental remediation. The present study emphasizes that thermally synthesized hematite nanomaterials can serve as low-cost, simple, stable, nontoxic, and visible-light photocatalysts that can be used as magnetic nano-catalysts.

Data availability

All data collected for this article are presented in figures. However, the data will be made available from the authors upon request.

Author contribution

Material preparation, major data collection and analysis were performed by SK. TS was involved in some data collections while AAA and EA were involved in some data curation. AB conceptualized the problem and designed the study. The draft of the manuscript was written by SK and finalized by AB. All authors reviewed the final manuscript.

Conflicts of interest

Authors declare that they have no conflict of interest.

Acknowledgements

References

1 U. Schwertmann and R. M. Cornell, *Iron Oxides in the Laboratory: Preparation and Characterization*, John Wiley & Sons, 2008.

2 Y. H. Chen and C. C. Lin, *Phys. Chem. Miner.*, 2014, **41**, 727–736.

3 W. Wu, Z. Wu, T. Yu, C. Jiang and W.-S. S. Kim, *Sci. Technol. Adv. Mater.*, 2015, **16**, 23501.

4 H. Wan, L. Hu, X. Liu, Y. Zhang, G. Chen, N. Zhang and R. Ma, *Chem. Sci.*, 2023, **14**, 2776–2798.

5 S. Kundu, T. Sarkar, G. Ghorai, P. K. Sahoo, A. A. Al-Ahmadi, A. Alghamdi and A. Bhattacharjee, *ACS Omega*, 2024, **9**, 22607–22618.

6 K. G. Gareev, *Magnetochemistry*, 2023, **9**, 119.

7 P. E. Swastika, H. Ardiyanti, D. L. Puspitarum, N. I. Istiqomah, N. A. Wibowo and E. Suharyadi, *Sens. Int.*, 2024, 100288, DOI: **10.1016/j.sintl.2024.100288**.

8 M. Islam, S. Kumar, N. Saxena and A. Nafees, *ChemistrySelect*, 2023, **8**, e202301048.

9 H. Kumari, S. Sonia, R. Ranga, S. Chahal, S. Devi, S. Sharma, S. Kumar, P. Kumar, S. Kumar, A. Kumar and R. Parmar, *Water, Air, Soil Pollut.*, 2023, **234**, 349.

10 M. F. Lanjwani, M. Tuzen, M. Y. Khuhawar and T. A. Saleh, *Inorg. Chem. Commun.*, 2024, **159**, 111613.

11 S. Lotfi, M. El Ouardi, H. A. Ahsaine and A. Assani, *Catal. Rev.*, 2024, **66**, 214–258.

12 S. Singh, A. Kumar, N. Kataria, S. Kumar and P. Kumar, *J. Environ. Chem. Eng.*, 2021, **9**, 106266.

13 M. Buaisha, S. Balku and S. Özalp-Yaman, *Civ. Eng. J.*, 2020, **6**, 470–477.

14 A. R. A. Scharnberg, A. C. De Loreto and A. K. Alves, *Emerg. Sci. J.*, 2020, **4**, 11–17.

15 I. Ibrahimi, N. Deva and S. Mehmeti, *Civ. Eng. J.*, 2020, **6**, 907–918.

16 P. Dutta, M. Rabbi, M. A. Sufian and S. Mahjebin, *Eng. Appl. Sci. Lett.*, 2022, **5**, 1.

17 A. P. Periyasamy, *Sustainability*, 2024, **16**, 495.

18 R. Al-Tohamy, S. S. Ali, F. Li, K. M. Okasha, Y. A.-G. Mahmoud, T. Elsamahy, H. Jiao, Y. Fu and J. Sun, *Ecotoxicol. Environ. Saf.*, 2022, **231**, 113160.

19 M. K. H. M. Nazri and N. Sapawe, *Mater. Today: Proc.*, 2020, **31**, A42–A47.

20 G. D. Sharma, P. Balraju, M. Kumar and M. S. Roy, *Mater. Sci. Eng. B*, 2009, **162**, 32–39.

21 G. Sriram, S. Thangarasu, K. Selvakumar, M. Kurkuri, N. R. Dhineshbabu and T. H. Oh, *Colloids Surf., A*, 2024, **685**, 133199.

22 A. Khatri and P. S. Rana, *Phys. B*, 2020, **579**, 411905.

23 J. A. Buledi, A. Hyder, A. Ali, A. R. Solangi, A. Mallah, S. Amin, A. A. Memon, K. H. Thebo and M. Kazi, *J. Phys. Chem. Solids*, 2024, **192**, 112083.

24 M. Vinuth, H. S. B. Naik, B. M. Vinoda, S. M. Pradeepa, G. A. Kumar and K. C. Sekhar, *J. Environ. Anal. Toxicol.*, 2016, **6**, 1000355.

25 A. Kumar, C. J. Raorane, A. Syed, A. H. Bahkali, A. M. Elgorban, V. Raj and S. C. Kim, *Environ. Res.*, 2023, **216**, 114741.

26 F. Sako, N. Taniguchi, N. Kobayashi and E. Takakuwa, *Toxicol. Appl. Pharmacol.*, 1977, **39**, 111–117.

27 F. Sako, N. Kobayashi, H. Watabe and N. Taniguchi, *Toxicol. Appl. Pharmacol.*, 1980, **54**, 285–292.

28 S. K. Bhar, S. Jana, A. Mondal and N. Mukherjee, *J. Colloid Interface Sci.*, 2013, **393**, 286–290.

29 M. Farbod and M. Khademalrasool, *Powder Technol.*, 2011, **214**, 344–348.

30 K. Vignesh, R. Hariharan, M. Rajarajan and A. Suganthi, *Solid State Sci.*, 2013, **21**, 91–99.

31 R. Satheesh, K. Vignesh, A. Suganthi and M. Rajarajan, *J. Environ. Chem. Eng.*, 2014, **2**, 1956–1968.

32 D. S. Chaudhari, R. P. Upadhyay, G. Y. Shinde, M. B. Gawande, J. Filip, R. S. Varma and R. Zbořil, *Green Chem.*, 2024, **26**, 7579–7655.

33 F. T. Geldasa, M. A. Kebede, M. W. Shura and F. G. Hone, *RSC Adv.*, 2023, **13**, 18404–18442.

34 S. Yadav, K. Shakya, A. Gupta, D. Singh, A. R. Chandran, A. Varayil Aanappalli, K. Goyal, N. Rani and K. Saini, *Environ. Sci. Pollut. Res.*, 2023, **30**, 71912–71932.

35 C. C. Nguyen, N. N. Vu and T.-O. Do, *J. Mater. Chem. A*, 2015, **3**, 18345–18359.

36 S. Chahal, N. Rani, A. Kumar and P. Kumar, *Vacuum*, 2020, **172**, 109075.

37 F. Zhang, X. Wang, H. Liu, C. Liu, Y. Wan, Y. Long and Z. Cai, *Appl. Sci.*, 2019, **9**, 2489.

38 H. Tong, S. Ouyang, Y. Bi, N. Umezawa, M. Oshikiri and J. Ye, *Adv. Mater.*, 2012, **24**, 229–251.

39 G. Ren, H. Han, Y. Wang, S. Liu, J. Zhao, X. Meng and Z. Li, *Nanomaterials*, 2021, **11**, 1804.

40 C. N. C. Hitam and A. A. Jalil, *J. Environ. Manag.*, 2020, **258**, 110050.

41 A. Alharbi and E. A. Abdelrahman, *Spectrochim. Acta, Part A*, 2020, **226**, 117612.

42 L. Li, Y. Chu, Y. Liu and L. Dong, *J. Phys. Chem. C*, 2007, **111**, 2123–2127.

43 A. Ashraf, R. Wahab, A. A. Al-Khedhairy, A. Khan and F. Rahman, *Mater. Chem. Phys.*, 2024, **316**, 129111.

44 M. B. Goudjil, H. Dali, S. Zighmi, Z. Mahcene and S. E. Bencheikh, *Desalin. Water Treat.*, 2024, 100079.

45 S. Sagadevan, R. P. Sivasankaran, J. A. Lett, I. Fatimah, G. K. Weldegebrieal, E. Léonard, M.-V. Le and T. Soga, *Symmetry*, 2023, **15**, 1139.

46 A. Pathan, S. H. Bhatt, S. Vajapara and C. P. Bhasin, *Int. J. Thin Film Sci. Technol.*, 2022, **11**, 213–224.

47 A. M. Alenad, M. S. Waheed, S. Aman, N. Ahmad, A. R. Khan, R. Y. Khosa, M. Z. Ansari, S. A. Khan, H. M. T. Farid and T. A. M. Taha, *Mater. Res. Bull.*, 2023, **165**, 112306.

48 S. Rehman, F. Ahmed, M. U. A. Khan, A. Aljaafari, S. Manickam and P. L. Show, *Chem. Eng. Process.*, 2022, **175**, 108909.

49 A. D. Khalaji, *Phys. Chem. Res.*, 2022, **10**, 473–483.

50 M. Sharmila, R. J. Mani, C. Parvathiraja, S. M. A. Kader, M. R. Siddiqui, S. M. Wabaidur, M. A. Islam and W.-C. Lai, *Water*, 2022, **14**, 2301.

51 G. K. Weldegebrieal and A. K. Sibhatu, *Optik*, 2021, **241**, 167226.

52 H. Liu, Z. Wang, H. Li, H. Wang and R. Yu, *Mater. Res. Bull.*, 2018, **100**, 302–307.

53 R. K. Shah, *Arabian J. Chem.*, 2023, **16**, 104444.

54 A. Lassoued, *J. Mol. Struct.*, 2021, **1239**, 130489.

55 M. R. Joya, J. B. Ortega, J. O. D. Malafatti and E. C. Paris, *ACS Omega*, 2019, **4**, 17477–17486.

56 X. Liu, K. Chen, J.-J. Shim and J. Huang, *J. Saudi Chem. Soc.*, 2015, **19**, 479–484.

57 Y. Xu, G. Zhang, Y. Du, Y. Sun and D. Gao, *Mater. Lett.*, 2013, **92**, 321–324.

58 R. M. Hegazey, E. A. Abdelrahman, Y. H. Kotp, A. M. Hameed and A. Subaihi, *J. Mater. Res. Technol.*, 2020, **9**, 1652–1661.

59 J. Sundaramurthy, P. S. Kumar, M. Kalaivani, V. Thavasi, S. G. Mhaisalkar and S. Ramakrishna, *RSC Adv.*, 2012, **2**, 8201–8208.

60 D. E. Fouad, C. Zhang, T. D. Mekuria, C. Bi, A. A. Zaidi and A. H. Shah, *Ultrason. Sonochem.*, 2019, **59**, 104713.

61 S. Suman, S. Chahal, A. Kumar and P. Kumar, in *AIP Conference Proceedings*, AIP Publishing, 2020, vol. 2265.

62 S. K. Maji, N. Mukherjee, A. Mondal and B. Adhikary, *Polyhedron*, 2012, **33**, 145–149.

63 S. Chahal, A. Kumar and P. Kumar, *Crystals*, 2020, **10**, 273.

64 A. M. Ali, M. A. Sayed, H. Algarni, V. Ganesh, M. Aslam, A. A. Ismail and H. M. El-Bery, *Catalysts*, 2021, **11**, 1062.

65 R. Z. Ahmed, S. E. Laouini, C. Salmi, A. Bouafia, S. Meneceur, H. A. Mohammed, S. Chihi, F. Alharthi and J. A. A. Abdullah, *Biomass Convers. Biorefin.*, 2023, 1–15.

66 S. Rajamohan, V. Kumaravel, A. Abdel-Wahab, S. Ayyadurai and R. Muthuramalingam, *Can. J. Chem. Eng.*, 2018, **96**, 1713–1722.

67 M. Imran, A. Abutaleb, M. A. Ali, T. Ahamad, A. R. Ansari, M. Shariq, D. Lolla and A. Khan, *Mater. Lett.*, 2020, **258**, 126748.

68 G.-Y. Zhang, Y. Feng, Y.-Y. Xu, D.-Z. Gao and Y.-Q. Sun, *Mater. Res. Bull.*, 2012, **47**, 625–630.

69 S. Kundu, T. Sarkar, G. Ghorai, M. Zubko, P. K. Sahoo, M. Weselski, V. R. Reddy and A. Bhattacharjee, *Appl. Phys. A: Mater. Sci. Process.*, 2023, **129**, 264.

70 S. Kundu, T. Sarkar and A. Bhattacharjee, *Appl. Phys. A: Mater. Sci. Process.*, 2023, **129**, 723.

71 H. Lin, C. P. Huang, W. Li, C. Ni, S. I. Shah and Y.-H. Tseng, *Appl. Catal., B*, 2006, **68**, 1–11.

72 H. Cheng, W. Wang, B. Huang, Z. Wang, J. Zhan, X. Qin, X. Zhang and Y. Dai, *J. Mater. Chem. A*, 2013, **1**, 7131–7136.

73 Z. Cui, L. Zhang, Y. Xue, Y. Feng, M. Wang, J. Chen, B. Ji, C. Wang and Y. Xue, *Int. J. Miner., Metall. Mater.*, 2022, **29**, 2221–2231.

74 S. P. Adhikari and A. Lachgar, *J. Phys.: Conf. Ser.*, 2016, **758**, 12017.

75 B. Y. Balarabe, M. N. I. Oumarou, A. S. Koroney, I. Adjama and A. R. I. Baraze, *J. Nanotechnol.*, 2023, **2023**, 1–12.

76 N. Sapawe, *New J. Chem.*, 2015, **39**, 6377–6387.

77 P. Nuengmatcha, A. Kuyyogsuy, P. Porrawatkul, R. Pimsen, S. Chanthai and P. Nuengmatcha, *Water Sci. Eng.*, 2023, **16**, 243–251.

78 E. F. Aboelfetoh, A. E. Aboubaraka and E.-Z. M. Ebeid, *J. Cluster Sci.*, 2023, **34**, 2521–2535.

79 J. Kaur and S. Singhal, *Phys. B*, 2014, **450**, 49–53.

80 M. Janus, E. Kusiak-Nejman and A. W. Morawski, *React. Kinet., Mech. Catal.*, 2012, **106**, 289–295.

81 Y. Meng, S. Xia, G. Pan, J. Xue, J. Jiang and Z. Ni, *Korean J. Chem. Eng.*, 2017, **34**, 2331–2341.

82 M. R. Azhar, H. R. Abid, H. Sun, V. Periasamy, M. O. Tadé and S. Wang, *J. Colloid Interface Sci.*, 2016, **478**, 344–352.

83 X. Liu, P. Lv, G. Yao, C. Ma, Y. Tang, Y. Wu, P. Huo, J. Pan, W. Shi and Y. Yan, *Colloids Surf., A*, 2014, **441**, 420–426.

84 H. Yang, T. An, W. Song, W. Cooper, H. Luo and X. Guo, *J. Hazard. Mater.*, 2010, **179**, 834–839.

85 C. Hinshelwood, *The Kinetics of Chemical Change in Gaseous Systems*, Clarendon Press, 1926.

86 S.-Y. Pung, W.-P. Lee and A. Aziz, *Int. J. Inorg. Chem.*, 2012, **2012**, 1–9.

87 L. Wang, L. Chang, B. Zhao, Z. Yuan, G. Shao and W. Zheng, *Inorg. Chem.*, 2008, **47**, 1443–1452.

88 Y. D. Kaldante, R. N. Shirsat and M. G. Chaskar, *Nanosyst.: Phys., Chem., Math.*, 2021, **12**, 773–782.

89 V. Archana, J. J. Prince and S. Kalainathan, *J. Nanomater.*, 2021, **2021**, 1–25.

90 S. Chahal, N. Rani, A. Kumar and P. Kumar, *Appl. Surf. Sci.*, 2019, **493**, 87–93.

91 I. Kir, S. E. Laouini, S. Meneceur, A. Bouafia and H. A. M. Mohammed, *Biomass Convers. Biorefin.*, 2023, 1–10.

92 G. G. Hasan, H. A. Mohammed, M. Althamthami, A. Khelef, S. E. Laouini and S. Meneceur, *J. Photochem. Photobiol., A*, 2023, **443**, 114874.

93 K. Anandan and V. Rajendran, *Mater. Sci. Eng. B*, 2015, **199**, 48–56.

94 H. Mashiko, T. Oshima and A. Ohtomo, *Appl. Phys. Lett.*, 2011, **99**, 241904.